Article

Optical Images of Molecular Vibronic Couplings from Tip-Enhanced Fluorescence Excitation Spectroscopy

Feifei Qiu,[||] Zu-Yong Gong,[||] Dongwei Cao, Ce Song, Guangjun Tian,* Sai Duan,* and Yi Luo*

Cite This: *JACS Au* 2022, 2, 150−158

Read Online

ACCESS | 📊 Metrics & More | 📄 Article Recommendations | 🔵 Supporting Information

ABSTRACT: Tip-based photoemission spectroscopic techniques have now achieved subnanometer resolution that allows visualization of the chemical structure and even the ground-state vibrational modes of a single molecule. However, the ability to visualize the interplay between electronic and nuclear motions of excited states, i.e., vibronic couplings, is yet to be explored. Herein, we theoretically propose a new technique, namely, tip-enhanced fluorescence excitation (TEFE). TEFE takes advantage of the highly confined plasmonic field and thus can offer a possibility to directly visualize the vibronic effect of a single molecule in real space for arbitrary excited states in a given energy window. Numerical simulations for a single porphine molecule confirm that vibronic couplings originating from Herzberg−Teller

(HT) active modes can be visually identified. TEFE further enables high-order vibrational transitions that are normally suppressed in the other plasmon-based processes. Images of the combination vibrational transitions have the same pattern as that of their parental HT active mode's fundamental transition, providing a direct protocol for measurements of the activity of Franck−Condon modes of selected excited states. These findings strongly suggest that TEFE is a powerful strategy to identify the involvement of molecular moieties in the complicated electron−nuclear interactions of the excited states at the single-molecule level.

KEYWORDS: *vibronic coupling, tip-enhanced fluorescence excitation, single-molecule imaging, plasmonic field, Franck−Condon activity*
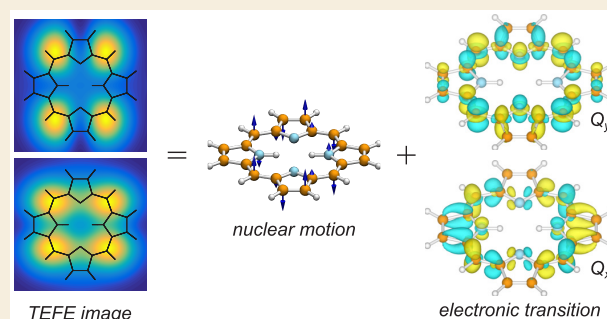
1. INTRODUCTION

Arising from the interaction between atomic and electronic motions, vibronic couplings are one of the key factors for understanding photochemical properties of molecular systems, including radiative/nonradiative decay,[1] charge transfer/transport,[2,3] intersystem crossing,[4] and so on. Vibronic couplings also play an essential role in almost all types of molecular spectroscopies, in particular with widespread weakly allowed or forbidden transitions.[5−7] Because of its importance, detailed investigations of the vibronic coupling effect, especially the involvement of molecular moieties, become highly desirable. However, because the vibronic coupling is nuclear coordinate-dependent in nature, the direct characterization of such an effect will require both submolecule spatial resolution (for atomic motions) and optical sensitivity (for electronic transitions), which cannot be achieved by conventional methods.

The combination of scanning tunneling microscopy (STM) and optical measurements has led to great successes in the real space optical characterization of single molecules with ultrahigh-resolution during the past two decades.[8−16] In particular, STM-based photoluminescence (STM-PL)[17,18] and tip-enhanced Raman scattering (TERS)[19−23] not only provide novel characterization protocols for molecular structures[24] but also bring exciting possibilities to break

down the optical selection rules,[25,26] which could significantly enrich our understanding of molecular properties. For instance, inspired by theoretical predictions,[27] the experimental visualization of molecular vibrations in real space has even been implemented with TERS recently.[22,23] Despite such great achievements, the direct real space measurement of the vibronic coupling effects in molecular excited states at the single-molecule level remains elusive because of the lack of appropriate methods.

One of the main difficulties to directly probe the excited-state properties in real space is that high-lying excited states normally have a very short lifetime (usually at the femtosecond to pisosecond scale[28−30]). This fact makes such states difficult to access with the commonly used luminescence-based techniques such as STM-PL. In principle, photon absorption measurements, which probe directly the electronic transitions, could be applied for such a purpose. However, the direct
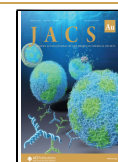
implementation of such measurements at the single-molecule level could be very challenging.

Herein, from a theoretical point of view, we propose a new protocol, namely, tip-enhanced fluorescence excitation (TEFE) spectroscopy, to circumvent this difficulty. TEFE can be considered as a technique analogous to STM-PL[17,18] but with frequency tunable excitations. In a very recent work, an essential experimental implementation of TEFE in an energy window around 0−0 transition in the first excited state of free-base phthalocyanine has indeed been reported by Imada et al.,[18] which demonstrated the experimental feasibility of TEFE. Our numerical validation confirms that TEFE can visualize the vibronic couplings between Herzberg−Teller (HT) modes and a specific electronic transition in real space. Moreover, the emergence of the high-order vibrational excitations in TEFE further provides a direct strategy for the measurements of the activity of Franck−Condon (FC) modes.

2. METHODOLOGY

2.1. Model

In order to demonstrate the working principle of the proposed TEFE method, we take a planar porphine molecule (H_2P) as an example. The working setup for the TEFE measurement is illustrated in Figure 1a, where a single H_2P molecule was confined in an optical cavity formed by a tip and a substrate. To minimize the fluorescence-quenching effect, a thin insulating spacer was introduced to decouple the molecule from the substrate.[8,10,11,32] Meanwhile, a so-called "pico-cavity" tip with an atomic protrusion in the tip apex was used in
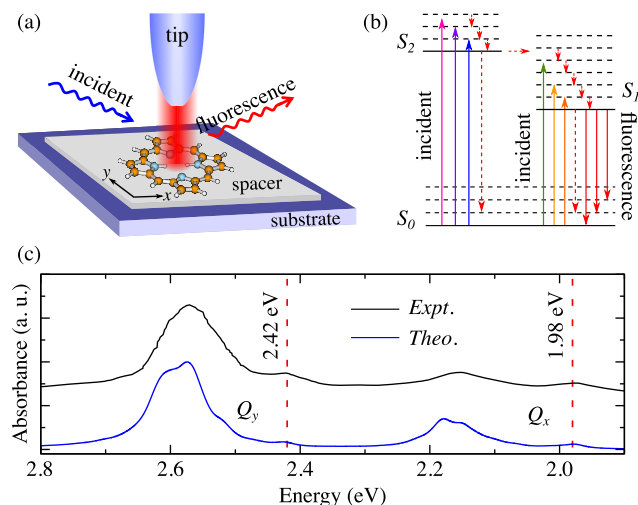

Figure 1. (a) Schematic picture of the proposed TEFE measurement of an H_2P molecule with an STM like setup. The molecule was supported by a thin spacer on the substrate to minimize the fluorescence quenching effect. The blue, yellow, and white balls represent N, C, and H atoms, respectively. The red cylinder between the tip and substrate represents the distribution of the plasmonic field. (b) Jablonski diagram for the fluorescence excitation process. Upward arrows indicate the excitation by incident light with different wavelengths. The vertical and horizontal dashed red arrows represent the vibrational decay and internal conversion between excited states, respectively. The downward arrows stand for the photon emission process. (c) Comparison of the calculated absorption spectrum of the H_2P molecule in the Q_x and Q_y bands with the experimental spectrum measured in the vapor phase. The experimental spectrum was adapted from ref 31, with permission from Elsevier. The calculated spectrum were broadened by a Lorentzian function with fwhm of 37.20 meV for a better comparison.

TEFE, where the possible fluorescence quenching effect caused by a smooth tip[33] could be significantly suppressed even with tip−molecule distance down to 0.37 nm.[17] Thus, we set the tip-induced fluorescence quenching as a constant at different tip positions. The macrocycle of the molecule was parallel to the substrate, which is the most probable adsorption configuration for such molecules.[34−36] The red cylinder between the tip and substrate represents the spatially confined plasmon (SCP) field generated in the STM nanocavity.

Figure 1b shows the corresponding Jablonski diagram of TEFE, where the solid and dashed horizontal black lines represent the electronic and vibrational states of the molecule, respectively. Similar to normal fluorescence excitation, the downward and horizontal red-dashed arrows represent the nonradiative decays (including both intrastate vibrational decay and interstate nonradiative decay) and internal conversion between excited states, respectively. These nonradiative energy relaxation processes are normally much faster than the radiative decay rate. Taking the H_2P molecule as an example, the nonradiative decays are about four orders faster than that of the radiative decay.[37] As a result, the fluorescence emission will be dominated by emissions from the ground vibrational level of the first excited state, i.e., a feature known as Kasha's rule,[38] as shown by the downward red-solid arrows in Figure 1b. It should be noted that the breakdown of Kasha's rule has been reported in several STM electroluminescence (STM-EL) measurements[10,14,15,39−41] because of the strong enhancement of the radiative channels in a plasmonic nanocavity.[42−45] We have thus checked the possible influences of the breakdown of Kasha's rule on the TEFE images of the H_2P molecule. Our numerical results via rate equation-based simulations reveal that the main features of the vibronic couplings for the H_2P molecule remain largely unchanged even when the non-Kasha's emissions are artificially increased by six orders because the fluorescence of the molecule is dominated by HT terms (see section S3 in Supporting Information for details).

The colored upward arrows represent the excitation of the molecule by the SCP field with different energies which, on the other hand, is different from the conventional excitation processes. In fact, it should be noted that SCP is highly confined in the optical cavity, which is essential for the visualization of the vibronic effect in TEFE.

2.2. TEFE Cross Section

TEFE measures the fluorescence cross section in the far field with different incident wavelengths at a specific tip position. In other words, both the spectral resonance and different enhancement for different vibrational modes that can be experimentally calibrated by dark-field scattering spectra[46] have been neglected in the practical simulations. Owing to the constant quantum efficiency as we assumed above, the observed cross section (the downward red-solid arrows in Figure 1b) is proportional to the absorbance of incident light. In this context, the TEFE cross section can be obtained as $\sigma \propto |\mu_{i,n \to f,n'}|^2$ with $\mu_{i,n \to f,n'} = \langle v_n | \langle \Psi_i | \mathcal{H}' | \Psi_f \rangle | v_{n'} \rangle$ being the transition matrix elements from vibrational level $|v_n\rangle$ in the initial electronic state $|\Psi_i\rangle$ to level $|v_{n'}\rangle$ in the final electronic state $|\Psi_f\rangle$.

In TEFE, the perturbation interaction Hamiltonian between the SCP and the molecule, i.e., $\mathcal{H}'$, plays an essential role. Previous studies have demonstrated that it is adequate to describe the interaction Hamiltonian by the minimal coupling Hamiltonian ($\mathcal{H}'_{min}$) for near-field scenarios,[47] where possible time-varying tunneling current could come into play.[48] In the Coulomb gauge, we have[26,47]

$$\mathcal{H}'_{min} = \mathbf{A} \cdot \hat{\mathbf{p}} \tag{1}$$

where $\mathbf{A}$ is the vector potential of SCP and $\hat{\mathbf{p}}$ is the momentum operator of electrons. The contributions from the magnetic field as well as high-order terms were neglected.

For convenience, $\mathcal{H}'_{min}$ can be transferred to the length gauge via the Power−Zienau−Woolley (PZW) transformation.[49] Specifically, we have

$$\mathcal{H}'_{\mathrm{mul}} = W^{-1}\mathcal{H}'_{\mathrm{min}}W$$
$$= \mathbf{P}\cdot\mathbf{E} \tag{2}$$

where $\mathbf{E}$ is the electric field and $\mathbf{P}$ is the electric polarization field defined as

$$\mathbf{P} = -(\mathbf{r}' - \mathbf{R}_0)\int_0^1 \delta(\mathbf{r} - \mathbf{R}_0 - \lambda(\mathbf{r}' - \mathbf{R}_0))\mathrm{d}\lambda \tag{3}$$

Here $W = \mathrm{e}^{i\mathbf{P}\cdot\mathbf{A}}$ is a unitary operator and $\mathbf{R}_0$ is a reference constant.

Nobusada and co-workers have found that $\mathcal{H}'_{\mathrm{mul}}$ could be further simplified for practical calculations.[50,51] In other words, by using the definition of the delta function and changing the integral order, one can easily find that the matrix element of

$$\mathcal{H}' = (\mathbf{r} - \mathbf{R}_0)\cdot\mathbf{E}_{\mathrm{eff}}(\mathbf{r} - \mathbf{R}_0) \tag{4}$$

is equivalent to that of $\mathcal{H}'_{\mathrm{mul}}$, where the effective plasmonic field is defined as $\mathbf{E}_{\mathrm{eff}}(\mathbf{r} - \mathbf{R}_0) = \int_0^1 \mathbf{E}(\mathbf{R}_0 + \lambda(\mathbf{r} - \mathbf{R}_0))\mathrm{d}\lambda$. It is worthwhile to mention that $\mathcal{H}'_{\mathrm{mul}}$ is identical to a more compact interaction Hamiltonian $\mathcal{H}' = \int_0^{\mathbf{r}} \mathbf{E}(\mathbf{r}', t)\cdot\mathrm{d}\mathbf{r}'$, when the transverse electric field effects were neglected.

Thus, the transition matrix elements can be rewritten as

$$\mu_{i,n\to f,n'} = \langle v_n|\mu_{i\to f}^{\mathrm{e}}|v_{n'}\rangle \tag{5}$$

with $\mu_{i\to f}^{\mathrm{e}} = \langle\Psi_i|(\mathbf{r} - \mathbf{R}_0)\cdot\mathbf{E}_{\mathrm{eff},0}(\mathbf{r} - \mathbf{R}_0)|\Psi_f\rangle$ being the electronic part. Here, $\mathbf{E}_{\mathrm{eff},0}$ is the amplitude of the effective plasmonic field. To make the transition matrix elements computable, we expand $\mu_{i\to f}^{\mathrm{e}}$ into a Taylor's series with respect to the vibrational normal coordinate Q_k around the equilibrium geometry $\mathbf{Q}_0$ as

$$\mu_{i\to f}^{\mathrm{e}} = \mu_{i\to f,0}^{\mathrm{e}} + \sum_k \mu_{i\to f,Q_k}^{\mathrm{e}'} Q_k \tag{6}$$

where $\mu_{i\to f,0}^{\mathrm{e}} = \mu_{i\to f}^{\mathrm{e}}(\mathbf{Q}_0)$ and $\mu_{i\to f,Q_k}^{\mathrm{e}'} = \left.\dfrac{\partial\mu_{i\to f}^{\mathrm{e}}}{\partial Q_k}\right|_{\mathbf{Q}_0}$. Here, the higher-order terms in the expansion were negelcted. The derivative term, i.e., $\mu_{i\to f,Q_k}^{\mathrm{e}'}$, clearly carries the information on the vibronic coupling that we would like to visualize in the present work. In fact, in the conventional excitation processes with the uniform external electromagnetic field, $\mu_{i\to f,Q_k}^{\mathrm{e}'}$ plays the key role in the spectral intensity for weak or forbidden transitions where the contributions of the first term are relatively small or even negligible.[5,52]

In the present work, we also want to suppress the contribution from the first term, i.e., the FC term, to better visualize the vibronic couplings. The ideal situation will be the scenario where $\mu_{i\to f,0}^{\mathrm{e}}$ equals or closes to 0. For a planar molecule with a cylinder plasmonic field, the point group of the whole system becomes C_s. In this context, all A′ excited states (antisymmetric with respect to the molecular plane) will be optically forbidden. For H_2P (D_{2h} without the plasmon, irreducible representation of the ground state is A_g), all A_g, B_{1g}, B_{2u}, and B_{3u} (in its original D_{2h} point group) excited states would become forbidden A′ states when the plasmonic field was taken into account. As a result, the FC contribution in the Q_x (B_{3u}) and Q_y (B_{2u}) bands can be naturally turned off, which allows the visualization of HT contributions in real space. In this case, the TEFE cross section becomes

$$\sigma \propto \left|\sum_k \mu_{i\to f,Q_k}^{\mathrm{e}'}\langle v_n|Q_k|v_{n'}\rangle\right|^2 \tag{7}$$

2.3. Computational Details

In practical calculations, only the dominant z-component of the SCP field was considered.[22] For the sake of simplification, $\mathbf{R}_0$ has been set to be the center of the plasmonic field. In this context, if the amplitude of the electric field decays exponentially from the plasmonic center, $\mathbf{E}_{\mathrm{eff},0}$ will also decay from the center (Figure S5). To this end, in the current work, $\mathbf{E}_{\mathrm{eff},0}$ was modeled by three-

dimensional Gaussian functions with given width in the xy plane (finite exponents α_x and α_y) but homogeneous along the z-direction ($\alpha_z = 0$),[53] which is a good approximation even with the consideration of the molecular self-interaction effect.[54] In the current calculations, $\mathbf{E}_{\mathrm{eff},0}$ was considered as an operator inside the integral of the transition matrix elements (see eq 5), which naturally captures the coupling between the electric-field-gradient and the molecular quadrupole as well as all other higher-order terms.[55]

Previous STM-PL work has shown that the size of the plasmonic field can be well-fitted by the relationship of $\sqrt{Rd}$ with R being the radius of the tip and d the tip−substrate distance.[17] In our simulations, we considered the so-called "pico-cavity" for the generation of plasmon and ultrathin insulator layers for decoupling, both of which were successfully applied in previous experiments.[8,56] Our test calculations manifest that a 4 Å tip−molecule distance is sufficient to avoid significant influences of the tip on the electronic transition properties of H_2P (Figure S6). As a result, R and d were set to 3 and 8 Å (by assuming the thickness of the decoupling layer to be 4 Å), respectively, which gives plasmonic confinement (α_x and α_y) of 5 Å. Because the size of the molecule is much smaller than that of the whole tip−substrate junction, the confinement of the SCP field is set to be constant during the movement of the tip positions, which is consistent with previous theoretical[54] and experimental[17] studies.

We used density functional theory (DFT) and time-dependent density functional theory (TDDFT) at the ωB97X-D/6-31G(d)[57,58] level as implemented in the Gaussian 16 program[59] to calculate the equilibrium geometries and vibrational frequencies of the molecule in the ground and excited states. The first two singlet excited states, S_1 and S_2, have been considered for Q_x and Q_y bands, respectively. The "First-principles Approaches for Surface and Tip Enhanced Raman Scattering (FASTERS)" program[60] was applied to calculate the transition electronic dipole moment of the molecule under the influence of the SCP. The required derivatives were then computed numerically by finite differential with a step size of 0.001 Å.

To efficiently compute the vibrational integrals, we have adopted the linear-coupling model (LCM).[3,61] LCM is a good approximation for rigid molecules such as H_2P and can simplify greatly the calculation of the multidimensional vibrational integrals. Our test calculations confirmed that LCM can nicely reproduce the exact absorption spectra for the two bands investigated in the present work (Figure S7). In the simulations we have neglected the finite temperature effect because the STM-PL experiments were efficiently performed only under cryogenic temperatures.[17,18] The vibrational integrals were computed with the DynaVib software.[62]

Finally, Lorentzian functions were applied for the broadening of the TEFE spectra, and the image was then constructed by the contrast of spectral cross sections at different tip positions (see eq S17 and section S5 in Supporting Information). Specifically, the TEFE spectra and images in Figure 2 were broadened with a full-width at half-maximum (fwhm) of 5.00 meV. For high-order vibrational transitions, a smaller fwhm of 0.50 meV, which has been obtained very recently in STM-based photoluminescence excitation spectroscopy,[18] was used to better locate the weak combinational transitions.

3. RESULTS AND DISCUSSION

3.1. Absorption of H$_2$P in Free Space

We first calculate the vibrationally resolved absorption spectrum of H_2P in the gas phase to validate the computational method. The theoretical spectrum containing both Q_y ($S_0 \to S_2$) and Q_x ($S_0 \to S_1$) bands (Figure 1c) is in excellent agreement with the experimental counterpart,[31] which manifests the accuracy of the calculations. Further analysis reveals that the FC terms only have contributions to the weak 0−0 bands located at 2.42 and 1.98 eV for Q_y and Q_x bands (dashed lines in Figure 1c), respectively. Other intense vibronic bands are dominated by the HT terms (Figure S8). It is worthwhile to mention that the relatively large energy gap
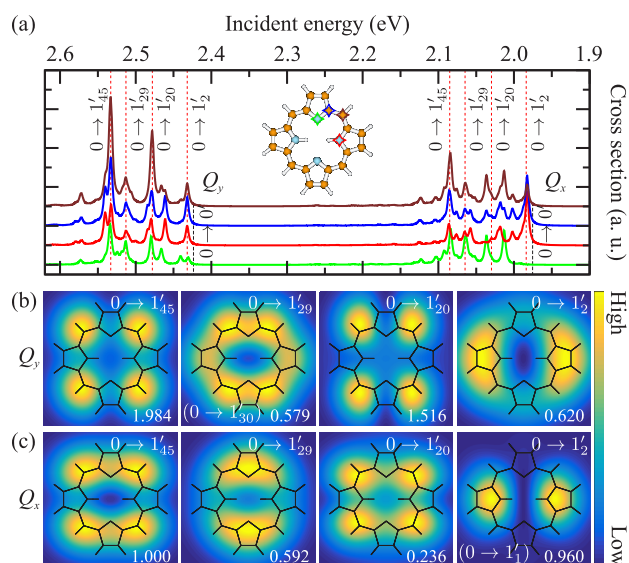
Figure 2. (a) TEFE spectra of H_2P obtained by placing the tip at different lateral positions (as indicated by the insets) on top of the molecule. TEFE images for selected TEFE peaks in the Q_y and Q_x bands as indicated in panel a are shown in panels b and c, respectively. The images were normalized to the $0 \to 1'_{45}$ transition in the Q_x band. The maximum value in each image is given at the bottom-right corner.

(0.44 eV) between the Q_y and Q_x bands makes the unambiguous visualization of the vibronic couplings in the corresponding excited states possible in the following discussions.

3.2. TEFE of H_2P from Fundamental Vibrational Transitions

We then move on to the calculation of the TEFE spectra. Figure 2a shows calculated results by placing the tip in four different lateral positions on top of the molecule as indicated by the inserted molecular model. In all spectra, the FC contributions, i.e., the 0−0 bands (black dashed lines in Figure 2a), were completely suppressed, which should be attributed to the reduced point group as mentioned above.

In the Q_y band, detailed analysis shows that there are four $0 \to 1'_i$ (here the subscript represents the index for the mode) fundamental vibrational transitions raised from the HT term which have significant contributions to all four spectra. Furthermore, calculated TEFE spectra are clearly dependent on the tip position. Specifically, the relative cross section of $0 \to 1'_{45}$ is reduced when the tip moves from above the bridge C to the N associated with H. The position dependence is more evident for the Q_x band. For instance, when the tip moves from on top of the bridge C to its neighboring C in the five-member ring, the most intense peak changes from $0 \to 1'_{45}$ to $0 \to 1'_2$. Because both bands contain only the HT contributions, the changes of the TEFE signal indicate that they could be capable of probing vibronic couplings in specific electronic states in real space.

To verify such a hypothesis, we first simulated the TEFE images for all four significant $0 \to 1'_i$ transitions in the intense Q_y band (Figure 2b). It should be mentioned that other transitions which are close in energy could also contribute to the images. Especially, the nearby mode of ν_{30} plays a very significant role in the $0 \to 1'_{29}$ image (a detailed analysis of the origin of the images reported in Figure 2 can be found in Figures S9 and S10).

The TEFE images of $0 \to 1'_{45}$ and $0 \to 1'_{20}$ are quite similar except for the slightly different locations of the exhibited four patterns. On the other hand, $0 \to 1'_{29}$ and $0 \to 1'_2$ have quite different patterns. For instance, the $0 \to 1'_{29}$ image forms a ring structure with the most bright lobes located on the C−C bonds in the methine groups, whereas $0 \to 1'_2$ displays a pair of bright lobes along the y-axis.

The vibronic coupling effect for the same vibration mode can vary when interacting with different electronic transitions and could cause changes to the resulting TEFE images. We then calculated the images for the Q_x band as shown in Figure 2c. It can be immediately noticed that the Q_x images have distinct features from their counterparts in the Q_y band. For instance, the bright lobes of $0 \to 1'_{45}$ are fused with each other along the x-axis, resulting in two patterns. Besides, the ringlike structure no longer holds in the $0 \to 1'_{29}$ image. Instead, a pair of bright lobes along the x-axis appears. For $0 \to 1'_{20}$ and $0 \to 1'_2$, although the patterns are similar, the subtle different locations as well as shapes guarantee that they are distinguishable from their counterparts in Q_y.

The different characters of the TEFE images shown in Figure 2 originate from the electronic state-dependent vibronic couplings, which, as we have mentioned, are faithfully associated with the interplay between the electronic transitions and nuclear motions. As shown in Figure 3a (a top view of the transition densities can be found in Figure S11), the transition
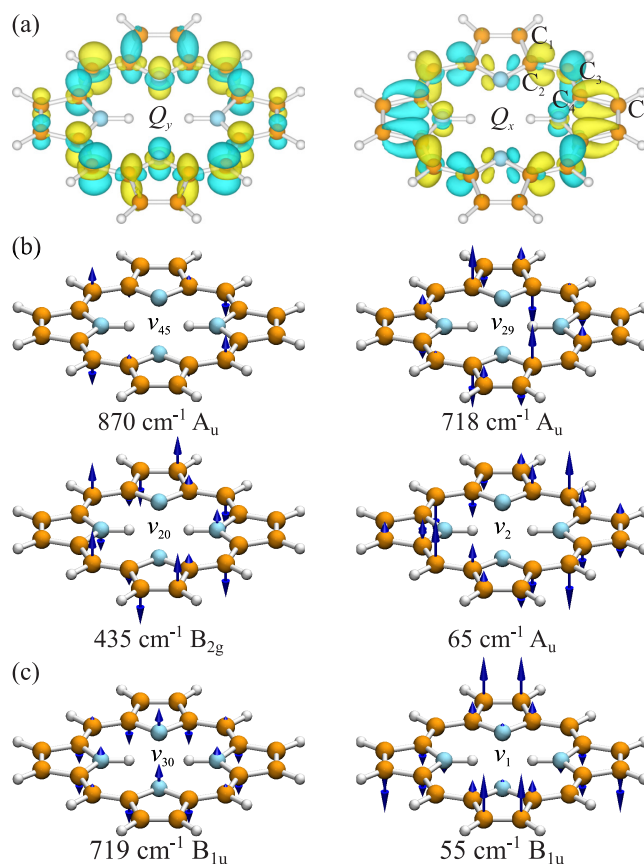

Figure 3. (a) Electronic transition density with isovalue of 0.003 for the Q_y and Q_x bands. (b) The four vibrational modes that are involved in the vibrational transitions for the TEFE images shown in Figure 2. (c) The two vibrational modes that have significant contributions to the $0 \to 1'_{29}$ image in the Q_y band and the $0 \to 1'_2$ image in the Q_x band, respectively.

densities for the two bands have similar characters except for a 90° rotation. The most significant differences can be found to be around the four N atoms and the outmost C atoms in the x (Q_y) and y (Q_x) directions. Some changes to the extension direction of the transition density around the bridging C atoms in the methyl group can also be found. Interestingly, such subtle changes can lead to quite different couplings with corresponding vibrations (all these modes are out-of-plane modes, Figure 3b; see the Supporting Information for more details).

For instance, ν_{45} is dominated by the nuclear motion of the C_3 atoms (definition of atomic labels can be found in Figure 3a). As a consequence, TEFE images for the $0 \rightarrow 1'_{45}$ transition in both Q_y and Q_x bands are most intense at the position of C_3, resulting in the bright lobes centered on methine groups (Figure 2ab). Furthermore, the second largest amplitudes of ν_{45} are located at C_2, which have an opposite phase with that of C_3. Although the phases of the electronic transitions at C_2 are the same, the extension directions in the Q_y and Q_x bands are toward C_1 and C_3, respectively, which lead to the localized and fused TEFE patterns. Because there are seldom electronic transitions on C_1, the phase matching between electronic transitions and nuclear motions associated with C_3 and C_2 again determine the patterns in TEFE images of the $0 \rightarrow 1'_{20}$ transition. In other words, the $0 \rightarrow 1'_{20}$ image in the Q_x band presents fusions along the x-axis, while it is more localized in the Q_y band.

It is noted that the images were constructed from spectral cross sections. Thus, nearby vibrational transitions could contribute to the image as well. For instance, the $0 \rightarrow 1'_{29}$ image in the Q_y band and the $0 \rightarrow 1'_2$ in the Q_x band contain contributions from the nearby modes of $0 \rightarrow 1'_{30}/0 \rightarrow 1'_{31}$ and $0 \rightarrow 1'_1$, respectively (Figures S9 and S10). The joint involvement of both ν_{29} and ν_{30} (Figure 3bc) is the key for the formation of the ringlike structure in the $0 \rightarrow 1'_{29}$ image.

Another key factor that could affect the spatial distribution and resolution of the TEFE images is the size of the plasmonic field. In the above simulations we have chosen the realistic size of 5 Å. It is expected, nevertheless, that a change to the field confinement should have notable influences on the TEFE images. To this end, we have also simulated the TEFE images for H_2P with different sized plasmonic fields (Figures S12–S14). For the images simulated with an ultrahighly confined field (a size of 2 Å), atomically resolved patterns can be clearly identified, while with a larger plasmonic size (8 Å), the main features are still reserved. These results indicate that TEFE could be applied to study the involvement of individual atoms in the complicated electron–nuclear interactions in real space, which could supply the foundations for the rational engineering of molecules.

3.3. TEFE of H₂P from High-Order Vibrational Transitions

Another important feature of the TEFE process when compared with the Raman process is that higher-order vibrational transitions, such as overtones and combinational transitions, could be more conveniently detected. Figure 4a shows the high-energy tail of a TEFE spectrum of the Q_x band, where several high-order vibrational transitions were identified.

For the current setup, as mentioned before, the only allowed fundamental vibrational transitions are the out-of-plane HT active modes ($0 \rightarrow 1'_{HT}$). Its transition matrix element can be written as (within LCM, details can be found in the Supporting Information)
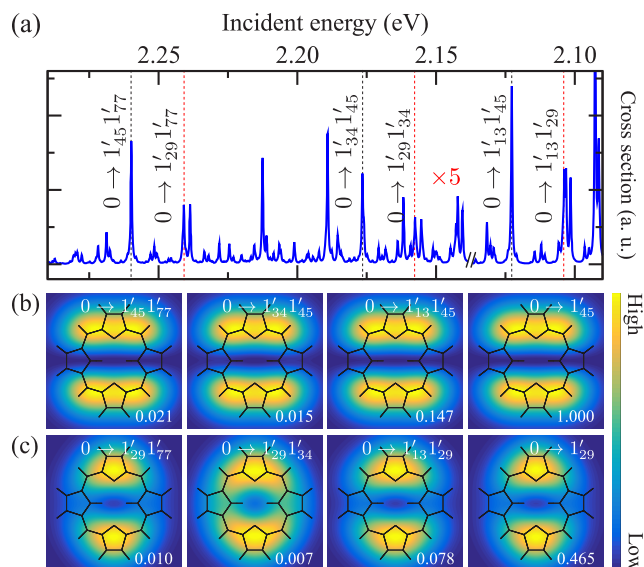

Figure 4. (a) The high-energy tail of the TEFE spectrum of the Q_x band as obtained on top of the N atom in the y-axis. (b and c) TEFE images of the combinational transitions involving modes ν_{45} and ν_{29}, respectively, as indicated by the dashed lines in panel a. Images for the fundamental transitions were also shown for comparison. The high-energy part of the TEFE spectrum in panel a has been scaled by 5. All images were normalized to the fundamental $0 \rightarrow 1'_{45}$ transition, and the maximum value in each image is given in the bottom-right corner.

$$\mu_{i,0 \rightarrow f, 1'_{HT}} = \mu^{e'}_{i \rightarrow f, Q_{HT}} \langle 0_{HT} | Q_{HT} | 1'_{HT} \rangle \prod_{l \neq HT} \langle 0_l | 0'_l \rangle \quad (8)$$

Interestingly, for second-order, the only allowed vibrational transitions are the combinational transitions of one HT mode with a totally symmetric FC mode ($0 \rightarrow 1'_{HT} 1'_{FC}$), which gives

$$\mu_{i,0 \rightarrow f, 1'_{HT} 1'_{FC}} = \mu^{e'}_{i \rightarrow f, Q_{HT}} \langle 0_{HT} | Q_{HT} | 1'_{HT} \rangle \langle 0_{FC} | 1'_{FC} \rangle$$
$$\times \prod_{l \neq HT, FC} \langle 0_l | 0'_l \rangle \quad (9)$$

One can immediately notice that eqs 8 and 9 share the same vibronic term of $\mu^{e'}_{i \rightarrow f, Q_{HT}}$. Thus, TEFE images of $0 \rightarrow 1'_{HT} 1'_{FC}$ would be identical to that of their parental $0 \rightarrow 1'_{HT}$ transition. Besides, we also have

$$\frac{\sigma_{0 \rightarrow 1'_{HT} 1'_{FC}}}{\sigma_{0 \rightarrow 1'_{HT}}} = \frac{|\langle 0_{FC} | 1'_{FC} \rangle|^2}{|\langle 0_{FC} | 0'_{FC} \rangle|^2} = S_{FC} \quad (10)$$

where S_{FC} is the famous Huang–Rhys factor[63] for the FC mode (see detailed derivation in the Supporting Information).

Numerical results shown in Figure 4bc demonstrate that TEFE images of $0 \rightarrow 1'_{45}$ and $0 \rightarrow 1'_{29}$ transitions in the Q_x band are indeed identical to their corresponding combination transitions, which provides a unique experimental protocol to visually identify the high-order modes. Moreover, Table 1 lists the cross section ratios of the TEFE images shown in Figure 4 together with the exact Huang–Rhys factors obtained from first-principles calculations. As anticipated, the cross section ratios agree very well with the exact Huang–Rhys factors, especially for the ratios associated with the intense $0 \rightarrow 1'_{45}$ transition. For that associated with $0 \rightarrow 1'_{29}$, the largest discrepancy between the ratios and the exact values is less than 15%, which should be further improved by the decrease of the vibrational dissipation rate.

Table 1. Comparison between the Cross Section Ratios and the Huang−Rhys Factors Obtained from First-Principles Calculations

ν_{FC}	$\dfrac{\sigma_{0 \to l'_{29} l_{FC}}}{\sigma_{0 \to l'_{29}}}$	$\dfrac{\sigma_{0 \to l'_{45} l_{FC}}}{\sigma_{0 \to l'_{45}}}$	S_{FC}
ν_{13}	0.167	0.147	0.147
ν_{34}	0.016	0.015	0.014
ν_{77}	0.021	0.021	0.021

The simple relation between TEFE of the high-order and fundamental vibrational transitions presents the potential of rendering out the Huang−Rhys factors for all of the totally symmetric modes with significant FC activity of a given electronic state, which could help greatly in our understanding of the fundamental electron−nuclear interactions in molecular systems.

3.4. Requirements for Experimental Implementation

As a theoretical prediction of a new technique, it would be helpful to discuss the possible conditions that are likely to play an important role in the experimental implementation. In fact, there are a few requirements for the proposed TEFE to be realized in experiments.

First, the molecule should be emissive, which is the same requirement for other luminescence-based techniques such as super-resolved fluorescence microscopy, STM-induced electroluminescence, and STM-PL. Because many types of molecules have been utilized in luminescence-based techniques, we expect that TEFE could find applications in similar ranges in diverse scenarios. Moreover, in TEFE the fluorescence quenching effect has to be minimized, which could be circumvented by introducing an atomistic protrusion at the tip apex and an atomically thin insulating spacer between the molecule and the substrate (as demonstrated in Figure 1a). Apparently, an increase in the distance between adsorbates and metallic substrates could suppress the quenching effect but also decrease the plasmonic confinement that is another decisive role for TEFE. Although the theoretical limit is ∼1 Å,[64] we expect that there would be optimal plasmonic confinement (probably around 5 Å as used in the present work), which counterbalances the resolution and intensity for TEFE in experiments.

Second, the proposed TEFE measurements will work more efficiently under ultrahigh vacuum (UHV) and low temperatures. UHV and low-temperature conditions can also significantly suppress the possible photobleaching effect and enable long-time (hour scale) measurement,[65] which is also a common requirement in ultrahigh-resolution techniques. For a 10×10 pixels mesh, if we assume a 3 s integration time at each grid point,[17] the time required to obtain all 8 images shown in Figure 2 is 0.67 h, which is indeed possible as demonstrated in the STM-induced electroluminescence experiments.[65] Under high temperatures,[10] thermally populated higher vibrational states and tautomerizations of the central hydrogen atoms in H_2P would come into play, which provide complex but abundant additional information about the single molecules.

Third, we have to emphasize that TEFE is analogous to the experimentally realized STM-PL with tunable light sources such as those recently used in tip-enhanced Raman excitation spectroscopy experiments.[66] The last requirement of efficient plasmon excitations under tunable wavelengths could be realized by using different tips that could form optical cavities with resonant energy in the whole ultraviolet−visible region.[10]

We note that, in a very recent work, Imada et al. successfully measured the PL excitation spectra of single phthalocyanine derivatives with STM.[18] Although only a rather narrow energy window has been considered, such an important experiment directly proved the viability of the TEFE measurements proposed in the present work.

Finally, we stress that although only a simple H_2P molecule with HT dominated optical transition properties was tested in the present work as a proof-of-principle model, TEFE has the potential to be extended to a wide range of molecular systems where the FC term comes into play. For these more general cases, the SCP field in the STM nanocavity might be inhomogeneous in all three directions and the x- and y-components of the field could also contribute to the TEFE cross section. Thus, the symmetry of the whole system could be further reduced to C_1. As a result, eq 6, including both FC and HT terms, should be evaluated, which offers the possibility to study the general transition properties between molecular ground and excited states (especially high-lying excited states other than S_1). One particularly interesting case under such general conditions is that more high-order transitions such as the combinational transitions involving a pair of FC active modes will be active in the TEFE process, which allows the detailed analysis of vibrational transitions that share the same vibronic peak but have different vibronic coupling properties. Moreover, the involvement of the FC modes in general cases would lead to significant influences of non-Kasha's emissions on the TEFE spectra and images. As we discuss in section S3 in the Supporting Information, the hot emissions from the excited vibrational levels of FC modes with strong activity could dramatically change the detected fluorescence signals with different incident frequencies, which provides an indication of non-Kasha's emissions in TEFE processes.

We believe that TEFE can be readily implemented in experiments and provide a general means in the investigation of excited-state optical properties at the single-molecule level for a wide range of molecular systems, which could supply a deep understanding of basic physical mechanisms, such as vibronic coupling effect and other electronic transition properties in the near future.

4. CONCLUSIONS

We theoretically proposed a new optical technique, termed TEFE, that utilizes the high spatial confinement of the plasmonic field. It was demonstrated that TEFE can enable the real space visualization of vibronic couplings that connect the electronic transitions and nuclear motions at the single-molecule level. TEFE provides a unique strategy to identify high-order vibrational transitions via its images. Moreover, the cross section ratios between the images for combination and fundamental vibrational transitions can accurately reproduce the Huang−Rhys factors of the totally symmetric modes in the selected electronic excited state. These fascinating features of TEFE open the door for investigating the spatial distribution of the excited state vibronic coupling, which allows identifying the involvement of each atom or chemical bond in different coupling regions.

■ ASSOCIATED CONTENT

ⓢ Supporting Information

The Supporting Information is available free of charge at https://pubs.acs.org/doi/10.1021/jacsau.1c00442.

Selection rules for the vibrational transitions, relation between the TEFE images of the fundamental and combinational transitions, influence of non-Kasha's rule emissions on the TEFE images, field distribution of $\mathbf{E}_{eff}$, transformation formula for TEFE images, influence of metallic tip on the absorption spectra of the H_2P molecule, validation of the LCM, analysis of the absorption spectrum of the molecule in free space, detailed assignment for the TEFE images, top view of the electronic transition density, and the influence of the field confinement on the TEFE images (PDF)

AUTHOR INFORMATION

Corresponding Authors

Guangjun Tian − *State Key Laboratory of Metastable Materials Science & Technology and Key Laboratory for Microstructural Material Physics of Hebei Province, School of Science, Yanshan University, Qinhuangdao 066004, P.R. China;* ◎ orcid.org/0000-0002-3915-300X; Email: tian@ysu.edu.cn

Sai Duan − *Collaborative Innovation Center of Chemistry for Energy Materials, Shanghai Key Laboratory of Molecular Catalysis and Innovative Materials, MOE Key Laboratory of Computational Physical Sciences, Department of Chemistry, Fudan University, Shanghai 200433, P.R. China;* ◎ orcid.org/0000-0002-3282-0711; Email: duansai@fudan.edu.cn

Yi Luo − *Hefei National Laboratory for Physical Sciences at the Microscale and Synergetic Innovation Center of Quantum Information & Quantum Physics, University of Science and Technology of China, Hefei 230026 Anhui, P.R. China;* Email: yiluo@ustc.edu.cn

Authors

Feifei Qiu − *State Key Laboratory of Metastable Materials Science & Technology and Key Laboratory for Microstructural Material Physics of Hebei Province, School of Science, Yanshan University, Qinhuangdao 066004, P.R. China*

Zu-Yong Gong − *Collaborative Innovation Center of Chemistry for Energy Materials, Shanghai Key Laboratory of Molecular Catalysis and Innovative Materials, MOE Key Laboratory of Computational Physical Sciences, Department of Chemistry, Fudan University, Shanghai 200433, P.R. China*

Dongwei Cao − *State Key Laboratory of Metastable Materials Science & Technology and Key Laboratory for Microstructural Material Physics of Hebei Province, School of Science, Yanshan University, Qinhuangdao 066004, P.R. China*

Ce Song − *Hefei National Laboratory for Physical Sciences at the Microscale and Synergetic Innovation Center of Quantum Information & Quantum Physics, University of Science and Technology of China, Hefei 230026 Anhui, P.R. China; Department of Theoretical Chemistry and Biology, School of Engineering Sciences in Chemistry, Biotechnology and Health, KTH Royal Institute of Technology, S-106 91 Stockholm, Sweden*

Complete contact information is available at:
https://pubs.acs.org/10.1021/jacsau.1c00442

Author Contributions

∥F.Q. and Z.-Y.G. contributed equally to this paper.

Notes

The authors declare no competing financial interest.

REFERENCES

(1) Franco, I.; Tretiak, S. Electron-Vibrational Dynamics of Photoexcited Polyfluorenes. *J. Am. Chem. Soc.* **2004**, *126*, 12130−12140.

(2) Falke, S. M.; Rozzi, C. A.; Brida, D.; Maiuri, M.; Amato, M.; Sommer, E.; De Sio, A.; Rubio, A.; Cerullo, G.; Molinari, E.; Lienau, C. Coherent Ultrafast Charge Transfer in an Organic Photovoltaic Blend. *Science* **2014**, *344*, 1001−1005.

(3) Tian, G.; Sun, D.; Zhang, Y.; Yu, X. Franck-Condon Blockade and Aggregation-Modulated Conductance in Molecular Devices Using Aggregation-Induced Emission-Active Molecules. *Angew. Chem., Int. Ed.* **2019**, *58*, 5951−5955.

(4) Gibson, J.; Monkman, A. P.; Penfold, T. J. The Importance of Vibronic Coupling for Efficient Reverse Intersystem Crossing in Thermally Activated Delayed Fluorescence Molecules. *ChemPhysChem* **2016**, *17*, 2956−2961.

(5) Small, G. J. Herzberg-Teller Vibronic Coupling and the Duschinsky Effect. *J. Chem. Phys.* **1971**, *54*, 3300−3306.

(6) Nafie, L. A.; Freedman, T. B. Vibronic Coupling Theory of Infrared Vibrational Transitions. *J. Chem. Phys.* **1983**, *78*, 7108−7116.

(7) Silverstein, D. W.; Jensen, L. Vibronic Coupling Simulations for Linear and Nonlinear Optical Processes: Theory. *J. Chem. Phys.* **2012**, *136*, 064111.

(8) Qiu, X. H.; Nazin, G. V.; Ho, W. Vibrationally Resolved Fluorescence Excited with Submolecular Precision. *Science* **2003**, *299*, 542−546.

(9) Dong, Z.-C.; Guo, X.-L.; Trifonov, A. S.; Dorozhkin, P. S.; Miki, K.; Kimura, K.; Yokoyama, S.; Mashiko, S. Vibrationally Resolved Fluorescence from Organic Molecules near Metal Surfaces in a Scanning Tunneling Microscope. *Phys. Rev. Lett.* **2004**, *92*, 086801.

(10) Dong, Z. C.; Zhang, X. L.; Gao, H. Y.; Luo, Y.; Zhang, C.; Chen, L. G.; Zhang, R.; Tao, X.; Zhang, Y.; Yang, J. L.; Hou, J. G. Generation of Molecular Hot Electroluminescence by Resonant Nanocavity Plasmons. *Nat. Photonics* **2010**, *4*, 50−54.

(11) Chen, C.; Chu, P.; Bobisch, C. A.; Mills, D. L.; Ho, W. Viewing the Interior of a Single Molecule: Vibronically Resolved Photon Imaging at Submolecular Resolution. *Phys. Rev. Lett.* **2010**, *105*, 217402.

(12) Zhang, Y.; Luo, Y.; Zhang, Y.; Yu, Y.-J.; Kuang, Y.-M.; Zhang, L.; Meng, Q.-S.; Luo, Y.; Yang, J.-L.; Dong, Z.-C.; Hou, J. Visualizing Coherent Intermolecular Dipole-Dipole Coupling in Real Space. *Nature* **2016**, *531*, 623.

(13) Doppagne, B.; Chong, M. C.; Lorchat, E.; Berciaud, S.; Romeo, M.; Bulou, H.; Boeglin, A.; Scheurer, F.; Schull, G. Vibronic Spectroscopy with Submolecular Resolution from STM-Induced Electroluminescence. *Phys. Rev. Lett.* **2017**, *118*, 127401.

(14) Kimura, K.; Miwa, K.; Imada, H.; Imai-Imada, M.; Kawahara, S.; Takeya, J.; Kawai, M.; Galperin, M.; Kim, Y. Selective Triplet Exciton Formation in a Single Molecule. *Nature* **2019**, *570*, 210−213.

(15) Doppagne, B.; Neuman, T.; Soria-Martinez, R.; López, L. E. P.; Bulou, H.; Romeo, M.; Berciaud, S.; Scheurer, F.; Aizpurua, J.; Schull, G. Single-Molecule Tautomerization Tracking through Space- and Time-Resolved Fluorescence Spectroscopy. *Nat. Nanotechnol.* **2020**, *15*, 207−211.

(16) Kong, F.-F.; Tian, X.-J.; Zhang, Y.; Yu, Y.-J.; Jing, S.-H.; Zhang, Y.; Tian, G.-J.; Luo, Y.; Yang, J.-L.; Dong, Z.-C.; Hou, J. G. Probing Intramolecular Vibronic Coupling through Vibronic-State Imaging. *Nat. Commun.* **2021**, *12*, 1280.

(17) Yang, B.; Chen, G.; Ghafoor, A.; Zhang, Y.; Zhang, Y.; Zhang, Y.; Luo, Y.; Yang, J.; Sandoghdar, V.; Aizpurua, J.; Dong, Z.; Hou, J. G. Sub-Nanometre Resolution in Single-Molecule Photoluminescence Imaging. *Nat. Photonics* **2020**, *14*, 693−699.

(18) Imada, H.; Imai-Imada, M.; Miwa, K.; Yamane, H.; Iwasa, T.; Tanaka, Y.; Toriumi, N.; Kimura, K.; Yokoshi, N.; Muranaka, A.; Uchiyama, M.; Taketsugu, T.; Kato, Y. K.; Ishihara, H.; Kim, Y. Single-Molecule Laser Nanospectroscopy with Micro−electron Volt Energy Resolution. *Science* **2021**, *373*, 95−98.

(19) Zhang, R.; Zhang, Y.; Dong, Z.; Jiang, S.; Zhang, C.; Chen, L.; Zhang, L.; Liao, Y.; Aizpurua, J.; Luo, Y.; Yang, J.; Hou, J. Chemical Mapping of a Single Molecule by Plasmon-Enhanced Raman Scattering. *Nature* **2013**, *498*, 82−86.

(20) Jiang, S.; Zhang, Y.; Zhang, R.; Hu, C.; Liao, M.; Luo, Y.; Yang, J.; Dong, Z.; Hou, J. Distinguishing Adjacent Molecules on a Surface Using Plasmon-Enhanced Raman Scattering. *Nat. Nanotechnol.* **2015**, *10*, 865.

(21) Zhang, R.; Zhang, X.; Wang, H.; Zhang, Y.; Jiang, S.; Hu, C.; Zhang, Y.; Luo, Y.; Dong, Z. Distinguishing Individual DNA Bases in a Network by Non-Resonant Tip-Enhanced Raman Scattering. *Angew. Chem., Int. Ed.* **2017**, *56*, 5561−5564.

(22) Lee, J.; Crampton, K. T.; Tallarida, N.; Apkarian, V. A. Visualizing Vibrational Normal Modes of a Single Molecule with Atomically Confined Light. *Nature* **2019**, *568*, 78.

(23) Zhang, Y.; Yang, B.; Ghafoor, A.; Zhang, Y.; Zhang, Y.-F.; Wang, R.-P.; Yang, J.-L.; Luo, Y.; Dong, Z.-C.; Hou, J. G. Visually Constructing the Chemical Structure of a Single Molecule by Scanning Raman Picoscopy. *Natl. Sci. Rev.* **2019**, *6*, 1169−1175.

(24) Duan, S.; Tian, G.; Ji, Y.; Shao, J.; Dong, Z.; Luo, Y. Theoretical Modeling of Plasmon-Enhanced Raman Images of a Single Molecule with Subnanometer Resolution. *J. Am. Chem. Soc.* **2015**, *137*, 9515−9518.

(25) Xie, Z.; Duan, S.; Wang, C.-K.; Luo, Y. Lighting up Long-Range Charge-Transfer States by a Localized Plasmonic Field. *Nanoscale* **2017**, *9*, 18189−18193.

(26) Duan, S.; Rinkevicius, Z.; Tian, G.; Luo, Y. Optomagnetic Effect Induced by Magnetized Nanocavity Plasmon. *J. Am. Chem. Soc.* **2019**, *141*, 13795−13798.

(27) Duan, S.; Tian, G.; Luo, Y. Visualization of Vibrational Modes in Real Space by Tip-Enhanced Non-Resonant Raman Spectroscopy. *Angew. Chem., Int. Ed.* **2016**, *55*, 1041−1045.

(28) Wei, T.; Huang, T.; Lin, H.; Lin, S. Lifetime Determination for High-Lying Excited States Using Z Scan. *Appl. Phys. Lett.* **1995**, *67*, 2266−2268.

(29) Gurzadyan, G. G.; Tran-Thi, T.-H.; Gustavsson, T. Time-Resolved Fluorescence Spectroscopy of High-Lying Electronic States of Zn-Tetraphenylporphyrin. *J. Chem. Phys.* **1998**, *108*, 385−388.

(30) Yu, H.-Z.; Baskin, J. S.; Zewail, A. H. Ultrafast Dynamics of Porphyrins in the Condensed Phase: II. Zinc Tetraphenylporphyrin. *J. Phys. Chem. A* **2002**, *106*, 9845−9854.

(31) Edwards, L.; Dolphin, D.; Gouterman, M.; Adler, A. Porphyrins XVII. Vapor Absorption Spectra and Redox Reactions: Tetraphenylporphins and Porphin. *J. Mol. Spectrosc.* **1971**, *38*, 16−32.

(32) Kuhnke, K.; Große, C.; Merino, P.; Kern, K. Atomic-Scale Imaging and Spectroscopy of Electroluminescence at Molecular Interfaces. *Chem. Rev.* **2017**, *117*, 5174−5222.

(33) Anger, P.; Bharadwaj, P.; Novotny, L. Enhancement and Quenching of Single-Molecule Fluorescence. *Phys. Rev. Lett.* **2006**, *96*, 113002.

(34) Bischoff, F.; Seufert, K.; Auwärter, W.; Joshi, S.; Vijayaraghavan, S.; Ecija, D.; Diller, K.; Papageorgiou, A. C.; Fischer, S.; Allegretti, F.; Duncan, D. A.; Klappenberger, F.; Blobner, F.; Han, R.; Barth, J. V. How Surface Bonding and Repulsive Interactions Cause Phase Transformations: Ordering of a Prototype Macrocyclic Compound on Ag (111). *ACS Nano* **2013**, *7*, 3139−3149.

(35) Diller, K.; Klappenberger, F.; Allegretti, F.; Papageorgiou, A.; Fischer, S.; Wiengarten, A.; Joshi, S.; Seufert, K.; Écija, D.; Auwärter, W.; Barth, J. V. Investigating the Molecule-Substrate Interaction of Prototypic Tetrapyrrole Compounds: Adsorption and Self-Metalation of Porphine on Cu(111). *J. Chem. Phys.* **2013**, *138*, 154710.

(36) Diller, K.; Klappenberger, F.; Allegretti, F.; Papageorgiou, A. C.; Fischer, S.; Duncan, D. A.; Maurer, R. J.; Lloyd, J. A.; Oh, S. C.; Reuter, K.; Barth, J. V. Temperature-Dependent Templated Growth of Porphine Thin Films on the (111) Facets of Copper and Silver. *J. Chem. Phys.* **2014**, *141*, 144703.

(37) Marcelli, A.; Foggi, P.; Moroni, L.; Gellini, C.; Salvi, P. R. Excited-State Absorption and Ultrafast Relaxation Dynamics of Porphyrin, Diprotonated Porphyrin, and Tetraoxaporphyrin Dication. *J. Phys. Chem. A* **2008**, *112*, 1864−1872.

(38) Kasha, M. Characterization of Electronic Transitions in Complex Molecules. *Discuss. Faraday Soc.* **1950**, *9*, 14−19.

(39) Chong, M. C.; Reecht, G.; Bulou, H.; Boeglin, A.; Scheurer, F.; Mathevet, F.; Schull, G. Narrow-Line Single-Molecule Transducer between Electronic Circuits and Surface Plasmons. *Phys. Rev. Lett.* **2016**, *116*, 036802.

(40) Chong, M. C.; Sosa-Vargas, L.; Bulou, H.; Boeglin, A.; Scheurer, F.; Mathevet, F.; Schull, G. Ordinary and Hot Electroluminescence from Single-Molecule Devices: Controlling the Emission Color by Chemical Engineering. *Nano Lett.* **2016**, *16*, 6480−6484.

(41) Tian, X.-J.; Kong, F.-F.; Yu, Y.-J.; Jing, S.-H.; Zhang, X.-B.; Liao, Y.; Zhang, Y.; Zhang, Y.; Dong, Z.-C. Plasmon-Enhanced S2 Electroluminescence from the High-lying Excited State of a Single Porphyrin Molecule. *Appl. Phys. Lett.* **2020**, *117*, 243301.

(42) Tian, G.; Liu, J.-C.; Luo, Y. Density-Matrix Approach for the Electroluminescence of Molecules in a Scanning Tunneling Microscope. *Phys. Rev. Lett.* **2011**, *106*, 177401.

(43) Tian, G.; Luo, Y. Electroluminescence of Molecules in a Scanning Tunneling Microscope: Role of Tunneling Electrons and Surface Plasmons. *Phys. Rev. B: Condens. Matter Mater. Phys.* **2011**, *84*, 205419.

(44) Chen, G.; Li, X.-G.; Zhang, Z.-Y.; Dong, Z.-C. Molecular Hot Electroluminescence due to Strongly Enhanced Spontaneous Emission Rates in a Plasmonic Nanocavity. *Nanoscale* **2015**, *7*, 2442−2449.

(45) Neuman, T.; Esteban, R.; Casanova, D.; García-Vidal, F. J.; Aizpurua, J. Coupling of Molecular Emitters and Plasmonic Cavities beyond the Point-Dipole Approximation. *Nano Lett.* **2018**, *18*, 2358−2364.

(46) Li, C.-Y.; Duan, S.; Wen, B.-Y.; Li, S.-B.; Kathiresan, M.; Xie, L.-Q.; Chen, S.; Anema, J. R.; Mao, B.-W.; Luo, Y.; Tian, Z.-Q.; Li, J.-F. Observation of Inhomogeneous Plasmonic Field Distribution in a Nanocavity. *Nat. Nanotechnol.* **2020**, *15*, 922−926.

(47) Rivera, N.; Kaminer, I.; Zhen, B.; Joannopoulos, J. D.; Soljačić, M. Shrinking Light to Allow Forbidden Transitions on the Atomic Scale. *Science* **2016**, *353*, 263−269.

(48) Zhu, W.; Esteban, R.; Borisov, A. G.; Baumberg, J. J.; Nordlander, P.; Lezec, H. J.; Aizpurua, J.; Crozier, K. B. Quantum Mechanical Effects in Plasmonic Structures with Subnanometre Gaps. *Nat. Commun.* **2016**, *7*, 11495.

(49) Babiker, M.; Power, E. A.; Thirunamachandran, T.; Stewartson, K. On a Generalization of the Power-Zienau-Woolley Transformation in Quantum Electrodynamics and Atomic Field Equations. *Proc. R. Soc. A* **1974**, *338*, 235−249.

(50) Iwasa, T.; Nobusada, K. Nonuniform Light-Matter Interaction Theory for Near-Field-Induced Electron Dynamics. *Phys. Rev. A: At., Mol., Opt. Phys.* **2009**, *80*, 043409.

(51) Iwasa, T.; Takenaka, M.; Taketsugu, T. Generalized Theoretical Method for the Interaction between Arbitrary Nonuniform Electric Field and Molecular Vibrations: Toward Near-Field Infrared Spectroscopy and Microscopy. *J. Chem. Phys.* **2016**, *144*, 124116.

(52) Herzberg, G.; Teller, E. Schwingungsstruktur Der Elektronenübergänge Bei Mehratomigen Molekülen. *Z. Phys. Chem., Abt. B* **1933**, *21B*, 410−446.

(53) Xie, Z.; Duan, S.; Wang, C.-K.; Luo, Y. Monitoring Hydrogen/ Deuterium Tautomerization in Transient Isomers of Single Porphine by Highly Localized Plasmonic Field. *J. Phys. Chem. C* **2019**, *123*, 11081−11093.

(54) Zhang, C.; Chen, B.-Q.; Li, Z.-Y. Optical Origin of Subnanometer Resolution in Tip-Enhanced Raman Mapping. *J. Phys. Chem. C* **2015**, *119*, 11858−11871.

(55) Hu, W.; Duan, S.; Luo, Y. Theoretical Modeling of Surface and Tip-Enhanced Raman Spectroscopies. *WIREs Computational Molecular Science* **2017**, *7*, e1293.

(56) Benz, F.; Schmidt, M. K.; Dreismann, A.; Chikkaraddy, R.; Zhang, Y.; Demetriadou, A.; Carnegie, C.; Ohadi, H.; de Nijs, B.; Esteban, R.; Aizpurua, J.; Baumberg, J. J. Single-Molecule Optomechanics in "Picocavities. *Science* **2016**, *354*, 726−729.

(57) Chai, J.-D.; Head-Gordon, M. Long-Range Corrected Hybrid Density Functionals with Damped Atom-Atom Dispersion Corrections. *Phys. Chem. Chem. Phys.* **2008**, *10*, 6615−6620.

(58) Rassolov, V. A.; Ratner, M. A.; Pople, J. A.; Redfern, P. C.; Curtiss, L. A. 6-31G* Basis Set for Third-Row Atoms. *J. Comput. Chem.* **2001**, *22*, 976−984.

(59) Frisch, M. J. et al. *Gaussian 16*, revision A.03; Gaussian Inc.: Wallingford, CT, 2016.

(60) Duan, S.; Tian, G.; Luo, Y. *First-Principles Approaches for Surface and Tip Enhanced Raman Scattering (FASTERS)*, ver 2.0; University of Science and Technology of China: China, 2020.

(61) Macak, P.; Luo, Y.; Ågren, H. Simulations of Vibronic Profiles in Two-Photon Absorption. *Chem. Phys. Lett.* **2000**, *330*, 447−456.

(62) Tian, G.; Duan, S.; Hua, W.; Luo, Y. *DynaVib*, ver. 1.0; Royal Institute of Technology: Sweden, 2012.

(63) Huang, K.; Rhys, A. Theory of Light Absorption and Non-Radiative Transitions in F-Centres. *Proc. R. Soc. London A* **1950**, *204*, 406−423.

(64) Atkin, J. M.; Raschke, M. B. Optical Spectroscopy Goes Intramolecular. *Nature* **2013**, *498*, 44−45.

(65) Zhang, L.; Yu, Y.-J.; Chen, L.-G.; Luo, Y.; Yang, B.; Kong, F.-F.; Chen, G.; Zhang, Y.; Zhang, Q.; Luo, Y.; Yang, J.-L.; Dong, Z.-C.; Hou, J. G. Electrically Driven Single-Photon Emission from an Isolated Single Molecule. *Nat. Commun.* **2017**, *8*, 580.

(66) Yang, M.; Mattei, M. S.; Cherqui, C. R.; Chen, X.; Van Duyne, R. P.; Schatz, G. C. Tip-Enhanced Raman Excitation Spectroscopy (TERES): Direct Spectral Characterization of the Gap-Mode Plasmon. *Nano Lett.* **2019**, *19*, 7309−7316.